Residual behavior of reinforced SFRC beams damaged by impact

Running Head: *Residual behavior of reinforced SFRC beams damaged by impact*

Carlos Zanuy[1], Gonzalo S.D. Ulzurrun

Department of Continuum Mechanics and Structures, ETS Ingenieros de Caminos, Universidad Politécnica de Madrid (UPM), Spain

Abstract

The awareness of damage caused by impacts in civil structures has increased during the last decades. Existing research has shown that impact strength of concrete structures can be improved with the addition of steel fibers, but little attention has been paid at the assessment of the structural condition after the impact. In fact, the residual capacity of reinforced SFRC (steel fiber-reinforced concrete) can be considered as one of the main advantages of the employ of SFRC in structures expected to suffer impact damage. The understanding of the residual capacity of impact-damaged structures, in terms of strength and energy absorption, might be decisive to safely perform evacuation and recovery operations, as well as evaluate rehabilitation tasks. This paper presents a research on the residual capacity of pre-impacted reinforced SFRC beams. Seven mixtures of SFRC are evaluated, including three types of steel fibers and two values of fiber amount (as well as companion unreinforced plain concrete mixture). The research includes an experimental campaign as well as a model to understand the contribution of

[1] Corresponding author; Tel.: +34 913366700; fax: +34 913366702.

Address: ETS Ingenieros de Caminos. c/ Profesor Aranguren, 3. 28040 Madrid, Spain.

E-mail address: carlos.zanuy@upm.es

the SFRC to the strength and ductility of undamaged and damaged specimens. Among the conclusions, it has been found out that the failure mode (i.e. shear- or flexure-governed) of damaged specimens depends on the crack pattern caused by the impact, and it can be different from the failure mode of undamaged specimens.

Keywords: Residual strength, impact, SFRC, reinforced concrete beams, shear strength, energy absorption.

Notation

b	=	beam width
c	=	depth of neutral axis
c_1	=	depth of uncracked concrete
d	=	effective depth
d_f	=	fiber diameter
f_c	=	concrete compressive strength
f_{ct}	=	concrete tensile strength
k	=	correction coefficient for the crack spacing
l_f	=	fiber length
s_{rm}	=	average crack spacing of reinforced concrete
s_{rm}	=	average crack spacing of reinforced SFRC
w	=	crack width
w_s	=	crack width at the level of the reinforcement
w_{sh}	=	diagonal crack width at the level of the reinforcement
x_{cr}	=	position of critical section
L	=	span length
M	=	bending moment
T_f	=	resultant force of normal stresses at diagonal crack

V	=	shear force
V_c	=	shear strength of concrete compression zone
V_f	=	shear strength due to crack-bridging stresses of SFRC
V_u	=	shear strength
ε_c	=	concrete strain
ε_{c0}	=	peak concrete strain
ε_{sm}	=	average steel strain
θ_c	=	angle of inclination of diagonal crack
σ_1	=	principal tensile stress
σ_2	=	principal compressive stress
σ_c	=	concrete stress
σ_{fm}	=	average normal stress at the diagonal crack
τ	=	shear stress
τ_m	=	shear stress at neutral axis
τ_{max}	=	maximum shear stress

1. Introduction

Concrete structures may suffer impacts during their service life due to either accidental (rockfall, vehicle collisions, tornado or earthquake debris) or provoked (terrorist attacks) actions. Under such impact loads, concrete structures have shown a high trend to develop brittle shear or punching failure modes [1-3]. Because such brittleness can lead to severe human or infrastructure damage, the benefits of adding fibers to the concrete has shown to be an interesting alternative for structures exposed to impacts. Zanuy et al. [4] have shown that the use of steel fiber-reinforced concrete (SFRC) can significantly increase the impact strength of concrete structures due to the higher energy absorption capacity, which can avoid shear-related failures in SFRC beams containing conventional longitudinal reinforcement and no stirrups (hereafter referred to as reinforced SFRC beams). Other authors [5,6] have also demonstrated the superior performance against impacts achieved with SFRC.

An interesting capability of reinforced SFRC elements arises when they do not completely collapse due to the impact, thereby allowing for evacuation of humans and recovery of goods after the impact event. Though existing research has mainly focused on the impact performance of concrete structures [4-6], it is also paramount to understand the residual capacity and ductility after impact in order to safely perform evacuation and recovery operations or even evaluate the possibility for rehabilitation.

Only few researchers have studied the residual capacity of concrete structures damaged by dynamic actions. Adhikary et al. [7] performed quasi-static tests on reinforced concrete beams previously subjected to drop-weight impacts. They proposed two indices (RRI: residual resistance index, RSI: residual stiffness index) to define the impact damage and they concluded a beneficial effect of high amount of transverse reinforcement, low longitudinal reinforcement ratio, and high concrete compressive strength. Bao and Li [8] have dealt with the residual

strength of blast-damaged reinforced concrete columns, concluding that a higher residual axial strength can be achieved by increasing the longitudinal and transverse reinforcing ratio.

The present paper focuses on the residual performance of impact-damaged reinforced SFRC beams. The use of SFRC is intended to not only improve the residual load carrying capacity, but more significantly the residual ductility. The research departs from the previous results obtained by Zanuy et al. [4][9], who tested 20 reinforced SFRC beams under drop-weight impact and companion quasi-static conditions. Seven SFRC mixtures were studied including three types of steel fibers and two volumetric amounts, in addition to a series of unreinforced plain concrete. The beams which did not fully collapse by the impact in the previous study have been subjected to quasi-static testing and the residual behavior is studied in the present paper.

2. Load carrying capacity of undamaged reinforced SFRC beams

It must be noted that this section is not intended to provide a general model to estimate the strength of reinforced SFRC beams. Available models have been already reported to estimate shear strength of such members [10,11], while the flexural capacity can be determined by means of sectional analysis. Rather, this section is aimed at understanding the mechanisms contributing to shear strength, especially in the post-yielding stage, where existing models have not focused on, but it has been a failure mode found in the tests presented in section 3.

2.1. Sectional analysis

The flexural response of a reinforced SFRC section can be obtained by a sectional analysis, using equilibrium and constitutive equations, and sectional compatibility (plain sections remain plane). In this contribution, sectional analysis is performed with an iterative method by dividing the cross-section into small thickness layers (Fig. 1a). For a given external bending moment, the solution in terms of strain distribution is searched, which requires two unknowns (e.g. neutral

axis position and curvature). The two equilibrium equations (integration of stresses equal to axial force and bending moment) are solved iteratively by means of the tangent method. The material behaviors are as represented in Fig. 1b. For SFRC in compression, the nonlinear stress-strain model proposed by Dhakal et al. [12] is used, as follows:

$$\sigma_c = f_c \frac{\left(\varepsilon_c / \varepsilon_{c0}\right)}{1-\left(\varepsilon_c / \varepsilon_{c0}\right)+\left(\varepsilon_c / \varepsilon_{c0}\right)^2} \quad (1)$$

where f_c is the compressive strength and ε_{c0} is the strain corresponding to f_c. Eq. (1) provides a unique expression for both pre- and post-peak stages of SFRC in compression. In tension, a linear pre-cracking stage is used with a bilinear post-cracking stage as suggested by Kooiman et al. [13]. The two lines of the softening stage are defined so that the area below the stress-crack width (σ_c-w) curve is the fracture energy (G_f) of the SFRC. The critical crack width is chosen as the 25% of the fiber length ($w_c = 0.25 l_f$), while the "corner" point is taken at a crack width of $w_0 = 0.1 w_c$. In order to calculate softening stresses, the crack width distribution has to be derived from the strain plane. It is here assumed a linear crack opening as represented in Fig. 1a, defined by the crack width at the level of the longitudinal reinforcement (w_s), which is obtained as follows:

$$w_s = \varepsilon_{sm} s_{rm} \quad (2)$$

where ε_{sm} is the average steel strain between two adjacent cracks (evaluated in a simplified way as 0.7 times the steel strain at the analyzed cracked section) and s_{rm} is the crack spacing. In order to introduce the positive influence of steel fibers on the crack spacing, the value calculated for reinforced concrete (s_r) is affected by a reduction coefficient k as suggested by [14,15]:

$$s_{rm} = s_r k \ , \ k = \frac{50}{l_f / d_f} \leq 1.0 \quad (3)$$

163 For the longitudinal steel reinforcement, a bilinear elastic-plastic model is considered (Fig. 1b).
164 The capabilities of the sectional model are analyzed in section 4.
165
166 *2.2. Shear strength model*
167
168 A shear strength model is introduced in this section in order to understand shear resisting
169 mechanisms of reinforced SFRC beams without stirrups and their remaining capacity after the
170 beams have been subjected to impact. In order to analyze shear resisting mechanisms, empirical
171 models for shear strength do not seem convenient even though they can provide good estimates
172 [11]. Therefore, a mechanical approach is necessary.
173
174 In general, shear strength of reinforced concrete beams without stirrups is a result of the
175 contribution of aggregate interlock/friction between diagonal crack surfaces, tangential stresses
176 at compression zone, dowel action and residual normal stresses of concrete along the diagonal
177 crack [16]. Some authors have proposed interesting approaches to integrate such contributions
178 [17-19]. Other models have shown to work rather well even by mainly focusing on one or two
179 of such resisting mechanisms only [20,21]. When using SFRC, the improvement of shear
180 strength comes from its crack-bridging capacity. On the one hand, the SFRC increases
181 significantly the contribution due to normal stresses developed along the diagonal crack. On the
182 other hand, it can help in keeping a small thickness of the diagonal crack, thereby providing
183 more friction between crack surfaces and dowel action capacity [10].
184
185 In the present approach, it is assumed that the shear strength of reinforced SFRC beams without
186 stirrups is mainly provided by tangential stresses developed at compression zone and normal
187 stresses at diagonal crack surfaces, which agrees with the suggestion by [10]. The model
188 consists of two stages: diagonal crack initiation and shear failure. The first stage is intended to
189 determine the position of the critical cross-section where shear failure initiates. The procedure to
190 determine the critical section follows the proposal by Gallego et al. [22]. The diagonal crack is

assumed to begin from an existing vertical (flexural) crack, where the normal stress distribution for a given bending moment is known according to section 2.1 (Fig. 2). When a diagonal crack does not yet exist, the shear force is assumed to be resisted by the uncracked zone only, which comprises the compression zone and the part subjected to tensile stresses where the tensile strength has not been reached, defined as c_1 in Fig. 2. The distribution of tangential stresses is considered parabolic, with the highest value (τ_m) at the neutral axis [17,22]. The resulting shear force is:

$$V_c = \frac{2}{3} b c_1 \tau_m \tag{4}$$

A diagonal crack opens when the principal tensile stress reaches the tensile strength at any point of the cross-section. The former requires the estimation of principal stresses along the section height from interaction of tangential and normal stresses, but Gallego et al. [22] concluded that very good estimates can be obtained by assuming that the point with highest principal stress is the neutral axis, where there is no normal stress. The Mohr's circle at that point is as plotted in Fig. 2: the principal tensile stress is equal to τ_m and its direction is inclined 45º with respect to the horizontal axis. Accordingly, the diagonal crack begins from the neutral axis of the critical section with an inclination of 45º. The instant of diagonal cracking takes place when the principal tensile stress ($\sigma_1 = \tau_m$) equals the tensile strength. To consider the biaxial stress state ($\sigma_2 = \sigma_1 = \tau_m$ in the Mohr's circle of Fig. 2), the tensile strength is reduced by the presence of the principal compressive stress by assuming a linear interaction between principal stresses in the tension-compression failure domain [23], as follows:

$$\sigma_1 = f_{ct}\left(1 - \frac{\sigma_2}{f_c}\right) \underset{\sigma_1=\sigma_2}{\Longrightarrow} \sigma_1 = \frac{f_{ct}}{1 + f_{ct}/f_c} \tag{5}$$

By introducing the principal tensile stress of Eq. (5) into Eq. (4), the shear force which leads to diagonal cracking is:

$$V_{cr} = \frac{2}{3} b c_1 \frac{f_{ct}}{1 + f_{ct} / f_c} \tag{6}$$

It should be noted that the shear/flexure interaction is included in (6) by the value of c_1 from the sectional analysis for a given moment (M). Therefore, V_{cr} can be calculated for each point of the moment-curvature diagram determined from sectional analysis as explained in section 2.1, and the corresponding position of the critical section (x_{cr} in Fig. 2) is obtained as follows for beams subjected to point loads (other loading arrangements can be solved by analogous analysis):

$$x_{cr} = \frac{M}{V_{cr}} \tag{7}$$

The solution is found at the section within the shear span ($x_{cr} \leq a$) with the minimum value of V_{cr}. For the elements studied in the present paper (refer to section 4.1), the critical section has been found at $x_{cr} = a$.

Once the critical section is found, the diagonal crack opens from the neutral axis of that section and extends towards the tensile reinforcement with an inclination of $\theta_c = 45^o$, as plotted in Fig. 3a. The shear strength is a result of tangential stresses at compression zone (V_c) and contribution of normal stresses at diagonal crack surfaces (V_f):

$$V_u = V_c + V_f \tag{8}$$

To calculate the contribution of the compression zone, it has to be noted that its size is reduced from c_1 at beginning of diagonal crack (Fig. 2) to c at failure (Fig. 3). Such reduction results in a redistribution of shear stresses which is assumed to lead to the parabolic distribution plotted in Fig. 3b. Accordingly, the capacity of the compression zone results:

242 $$V_c = \frac{2}{3} bc\tau_{\max} \tag{9}$$

243 The maximum principal tensile stress depends on the interaction between normal and tangential
244 stresses of Fig. 3b. The Mohr's circle at any point of the compression zone is as plotted in Fig.
245 3c, where the principal tensile stress can be obtained as follows:
246

247 $$\sigma_1 = -\frac{\sigma_c}{2} + \sqrt{\left(\frac{\sigma_c}{2}\right)^2 + \tau^2} \tag{10}$$

248 The highest capacity of V_c is reached when the largest σ_1 along the compression zone is equal to
249 the tensile strength of concrete (reduced to account for the biaxial stress state of Fig. 3c). As a
250 simplification, it is assumed that the largest σ_1 is obtained at the central point of the compression
251 zone, i.e. the point subjected to a shear stress τ_{max}. If the concomitant normal stress is $\sigma_c = \alpha f_c$ (to
252 be determined from sectional analysis), the following formulation is derived for the maximum
253 tangential stress:
254

255 $$\tau_{\max} = f_{ct}\sqrt{(1-\alpha)\left(1+\alpha+\alpha\frac{f_c}{f_{ct}}\right)} \tag{11}$$

256 Thus, the contribution of the compression zone is calculated by introducing Eq. (11) into Eq. (9)
257

258 Regarding the contribution of the SFRC along the diagonal crack (V_f), it can be calculated as the
259 vertical projection of the resultant of normal stresses T_f (Fig. 3d):
260

261 $$V_f = T_f \cos\theta_c = \sigma_{fm} b(d-c)\cot\theta_c \tag{12}$$

262 where σ_{fm} is the average normal stress of the SFRC along the diagonal crack surface. To
263 calculate such normal stresses, it is assumed a linear crack opening as represented in Fig. 3d,
264 from zero at the neutral axis (normal stress equal to f_{ct}) to w_{sh} at the level of the longitudinal

reinforcement. The value of w_{sh} can be calculated from the horizontal crack width at the reinforcement level (w in Fig. 3d) as follows:

$$w_{sh} = \frac{w}{\sin\theta_c} \tag{13}$$

where w can be derived from the steel strain at the section at $x = x_{cr}-(d-c)/\tan\theta_c$ (calculated by sectional analysis) analogously to Eq. (2). Due to the bilinear softening behavior of SFRC, the different situations plotted in Fig. 3e can occur, which is accounted for in the calculation of the average normal stress σ_{fm} to be introduced in Eq. (12).

Once the contribution provided by shear resisting mechanisms can be obtained from Eqs. (9) and (12), the following procedure has to be carried out to calculate the shear strength:

a. From sectional analysis, the bending moment-curvature diagram is obtained: this includes the calculation of distribution of normal stresses and strains for each bending moment M.
b. For each point of the diagram, terms V_c and V_s are calculated from the above equations, which provide the shear capacity of the section ($V_u = V_c + V_s$) under a given bending moment M.
c. The shear demand corresponding to each moment M is calculated as M/x_{cr}.
d. Shear failure takes place when the shear capacity is equal to the shear demand, which in turn provides the searched shear strength.

3. Experimental program

3.1. Overview

The experimental study has dealt with reinforced SFRC beams consisting of 2.0 m long prismatic specimens with a rectangular cross-section of 0.125 x 0.25 m (width x height). The

292 longitudinal reinforcement has consisted of two ribbed bars of 16 mm diameter at both the
293 bottom and the top, of conventional reinforcing steel B500SD [24]. The beams have contained
294 no stirrups, as represented in Fig. 4. Seven mixtures have been studied for the concrete, as listed
295 in Table 1. The material properties were tested at the age of beam tests. More details of material
296 characterization and manufacturing can be found in [9]. As it can be noted from Table 1,
297 specimens of series A were manufactured with plain concrete. The other series were made of six
298 mixtures of SFRC. Three types of steel fibers have been considered, namely short smooth
299 fibers, long hooked fibers and prismatic fibers (refer to [9] for further details). Two values of the
300 fiber volumetric content were studied: 0.5% and 1.0%, in addition to the reference plain
301 concrete of series A. The beams were tested in a three-point bending configuration with a clear
302 span length of 1.6 m (Fig. 4). More details about tests are provided in the next subsections.
303
304 *3.2. Reference tests of undamaged specimens*
305
306 Quasi-static tests were carried out by applying a load at midspan with stroke control at a rate of
307 0.1 mm/s on an undamaged beam of each series. Even though the quasi-static tests of
308 undamaged specimens have been exhaustively described in [4], a short summary is included
309 here for the sake of clarity of the present paper. Load-midspan displacement curves have been
310 plotted in Fig. 5 and the crack pattern of beams after quasi-static testing are represented in Fig.
311 6. The maximum applied load of each series, which will be considered as the undamaged
312 strength, is listed in Table 2.
313
314 The beam of series A failed by brittle shear before yielding of the longitudinal reinforcement.
315 The beams consisting of SFRC with 0.5% fiber amount failed by formation and development of
316 a shear crack when the longitudinal reinforcement had entered yielding stage: beam of series B
317 (prismatic fibers) failed right after beginning the yielding stage, while beams of series C and D
318 (hooked and smooth fibers, respectively) failed well after entering the plastification stage, when
319 the midspan deflection was 22 mm (L/73). In the tests of beams of series B, C and D, the shear

crack development resulted in a significant load release until a residual capacity of about 50 kN, as observed in Fig. 5. The capacity for energy absorption (area below the diagrams of Fig. 5) was rather high, as listed in Table 2. The increase of the fiber amount to 1.0% did not result in a significant strength gain, as the specimens with 0.5% fiber fraction already yielded, but a higher ductility and energy absorption capacity (see Table 2). Specimen of series E (prismatic fibers) failed by shear in a similar way as the specimen of series B, with the same fiber type and 0.5% volumetric amount, but the specimens of series F and G (hooked and smooth fibers, respectively) were able to deform until a midspan displacement larger than 40 mm (L/40) without any load release.

According to previous results, it can be concluded that the addition of 0.5% fiber fraction (series B, C and D) has resulted in an average strength increase of 49% with respect to the specimen without fibers (series A), but more significantly, it has allowed for reaching yielding of longitudinal reinforcement at midspan, thereby improving the energy absorption capacity. In addition, the increase of the fiber amount to 1.0% has further allowed for increasing the energy absorption capacity and developing a flexural failure, except for the specimen consisting of prismatic fibers. The results of quasi-static tests of undamaged beams will be used as a reference for the analysis of the damage caused by the impact.

3.3. Impact tests

For each studied series, two impact tests have been carried out. The tests were completed by freely dropping a steel mass of 200 kg to the top side of the midspan section from a height of 1.75 m (impact velocity = 5.9 m/s). Thus, the imparted input energy has been 3.4 kJ. A full description and analysis of impact tests has been reported in [4]. The main results are listed in Table 3 regarding impact strength (considered as the maximum registered total reaction at supports) and absorbed energy (area below the total-reaction-midspan deflection diagram), and a brief summary is provided next.

The specimens of series A (plain concrete) failed abruptly by shear failure with full development of diagonal cracks at shear spans, thereby showing the poor performance of reinforced concrete beams without stirrups against impact, which has been also demonstrated by other authors [2,3,25]. The specimens containing SFRC developed either a shear or flexural failure mode (refer to Table 3). In case a shear failure was obtained, it is considered a full collapse of the specimen because it was not possible to perform an additional test to evaluate the residual capacity. That was the case of one specimen of series B and C, with a 0.5% content of prismatic and hooked fibers, respectively. The other specimens, including all of the series containing 1.0% fiber amount, developed a flexural failure mode in the impact test, which indicated that they could still keep a certain residual carrying capacity.

The crack pattern after impact of those specimens having a flexural failure is represented in Fig. 7. Extensive cracking can be observed in the midspan region, including in some cases cracks which were not vertical but with an inclination larger than 45º with respect to the horizontal axis, which can be considered as the initiation of a shear plug. In addition, few very thin diagonal cracks also formed in the webs at shear spans. The former shows the beneficial effect of using SFRC: even though the tensile strength was reached at the webs, the crack bridging effect of steel fibers was able to avoid the diagonal crack progression and subsequent shear failure. In addition, extensive damage can be observed in the compression zone of the midspan region, which received the impact of the drop weight. The residual midspan deflection after impact testing is listed in Table 3, which oscillates between 9.1 mm (L/178) and 13.3 mm (L/120).

3.4. Residual tests

The specimens without a shear failure in impact tests have been subjected to a quasi-static test to evaluate the residual load carrying capacity and deformability. In all, 9 specimens have been

tested including at least one specimen of each series containing SFRC (series B to G). The specimens have been loaded in a three-point bending scheme under an imposed displacement at midspan at a rate of 0.1 mm/s, i.e. the same loading conditions as the corresponding quasi-static tests of undamaged specimens (section 3.2). The applied load was measured with a built-in load cell of the hydraulic actuator, and the midspan deflection has been recorded with a 100 mm range LVDT. No additional sensors were used in residual tests, because of the unavailability of other instrumentation employed in undamaged tests (see Fig. 4) after impact testing.

The crack patterns after residual tests are plotted in Fig. 7, together with the crack patterns prior to residual tests (i.e. after impact testing). As it can be noted, both shear and flexural failure modes have been obtained in residual tests, even for specimens of the same series (E and G). Actually, pure flexural failures were not found, but combined flexure/shear at midspan region with cracks inclined more than 45º due to pre-initiated shear plugs. Therefore, residual behavior will be referred to as brittle or ductile depending whether there was load release after peak load or not. Moreover, failure modes obtained in residual tests have been in some cases different than those obtained in quasi-tests of undamaged specimens (Fig. 6). Such observations indicate that the damage produced by the impact has played a significant influence in the result of residual tests. The load-midspan deflection diagrams of residual tests have been represented in Fig. 8 in comparison with the response of undamaged specimens. The residual deflection caused by the impact has been considered the origin for residual tests. The decrease in strength of impact-damaged specimens with respect to undamaged beams can be expressed with the RRI index proposed by Adhikary et al. [7], which is listed in Table 4. According to RRI obtained, the degree of damage caused by the impact can be classified as low (RRI > 0.8) in general, with even no damage for the beam of series F, and some higher damage for one beam of series E (medium according to [7] for 0.6 < RRI < 0.8). However, it is clear that RRI values do not inform about the residual failure mode or the residual energy absorption capacity.

403 The beam of series B developed a ductile behavior according to the load-deflection diagram,
404 with the response governed by widening of an existing crack at midspan with an inclination
405 larger than 45º and subsequent splitting crack at the level of the tensile reinforcement. Such
406 response was rather different from the corresponding undamaged specimen, with a shear failure
407 soon after yielding of the longitudinal reinforcement without post-peak ductility. It becomes
408 apparent that the crack pattern produced by the impact forced a critical section at midspan,
409 which had more ductility than a common shear crack development.
410
411 The beam of series C showed a very similar behavior to that described for beam B: ductile
412 failure by progression of an impact-caused crack at midspan, different from the shear failure
413 with limited post-peak ductility of the corresponding undamaged specimen.
414
415 The beams of series D developed a shear failure by full development of a diagonal crack at one
416 of the shear spans. Such beams did not have post-peak ductility and the response of the
417 corresponding undamaged specimen provides a good envelope for residual tests.
418
419 In tests of series E, one of the beams (E-STR-IMP-A-R) developed a shear failure without post-
420 peak ductility, rather similar to residual tests of series D, but the other beam (E-STR-IMP-A-R)
421 behaved like those of series B and C: ductile response governed by progressive opening of
422 inclined cracks at midspan.
423
424 The response of the beam of series F was also governed by the cracks caused by the shear plug
425 at midspan, showing no strength and ductility reduction with respect to the undamaged
426 specimen.
427
428 Finally, the two specimens of series G behaved differently. Beam G-STR-IMP-A-R failed by
429 shear with limited post-peak ductility, but the response of beam G-STR-IMP-B-R was governed

by pre-formed inclined (almost vertical) cracks at midspan due to the shear plug caused by the impact, thereby developing ductile response like the corresponding undamaged specimen.

According to experimental observations, it is clear that the damage caused by the impact was decisive in the residual response of tested specimens, especially regarding post-peak ductility and energy absorption capacity. It seems that when the impact causes a shear plug, the critical section is forced at midspan region, which can be more ductile than a shear-critical undamaged beam. Change of failure mode from brittle for undamaged specimens to ductile for impact-damaged specimens can be also observed from the experiments of reinforced concrete beams of [7] (series SR3.8-0.8) but no specific analysis was carried on.

4. Analysis of results

4.1. Resisting mechanisms of undamaged beams

The model presented in section 2 is employed to analyze the quasi-static response of undamaged specimens of series B to G. The compressive and tensile material properties used in the model are those obtained experimentally (Table 1). In this way, the particularities of tested SFRC mixtures are incorporated in the analysis and no further estimations are needed, except for the critical crack width in tension which depends on the fiber length ($w_c = 0.25l_f$). The comparison between experimental and model results is represented in Fig. 9. For each series B to G, the sectional response of the midspan section in terms of bending moment-strain diagrams is obtained (refer to the position of strain gage SG2 in Fig. 4). Such diagrams are preferred here to load-deflection curves because deflections are not directly obtained from the sectional analysis of section 2.1 and, thus, comparison between sectional analysis and experimental response would not be straightforward. The sectional analysis is carried out until failure is obtained by the model when the shear strength reaches the shear demand as explained in section 2.2. The corresponding diagrams representing shear capacity and shear demand are also plotted

458 in Fig. 9, where big points represent the experimental strength. As it can be observed, the
459 agreement between experimental and model results is very good.
460
461 The critical flexural section where shear failure initiates has been found below the load point
462 with the model described in section 2.2. The corresponding diagonal cracking load can be
463 compared with the experimental value, which could be detected by the use of two LVDTs
464 measuring the height variation at one section of each shear span as represented in Fig. 4. The
465 measurements taken at both LVDTs are represented in Fig. 10a. An interesting observation can
466 be made, that diagonal cracking occurred in tests of series F and G but they did not progress and
467 final failure mode was due to flexure. The finding that a diagonal crack initiated in all beams is
468 correctly reproduced by the model, and a comparison of experimental and model values of
469 cracking load is given in Fig. 10b.
470
471 Regarding failure mode, it is noted that all shear failures have occurred in the stage of yielding
472 of the longitudinal reinforcement, which requires the model ability to work in that strain range,
473 including the post-peak stage of SFRC in compression. The following conclusions can be drawn
474 from the analysis of experimental results with the model and the observations of Fig. 9. In the
475 particular case of specimens with prismatic fibers (series B and E), the model shows a
476 significant decrease of V_c when the compression zone starts to soften. Such result is due to the
477 reduction of τ_{max} under high compressive stresses at the midpoint of the compression zone (α
478 approaches 1.0 in Eq. (11)). The model indicates that such softening of the compression zone
479 occurs right after beginning of yielding of longitudinal reinforcement, which explains the
480 failure. Therefore, the load release at failure observed in the load-deflection diagrams of series
481 B and E in Fig. 8 seems to be due to the collapse of V_c. Similar results are obtained with the
482 model for specimens with hooked fibers (series C and F): a large reduction in V_c occurs when
483 the compression zone softens, but in these tests that takes place well within the yielding stage of
484 the longitudinal reinforcement. The reduction of V_c leads to failure of the beam of series C as
485 the shear demand reaches the shear capacity according to the model, but it is not enough to

collapse the beam of series F as the shear capacity provided by V_f is still able to resist the shear demand. Some differences in the behavior can be obtained with the model for the beams with smooth fibers (series D and G). In such cases, the reduction of V_c is more moderate and it even represents 50% of shear capacity at failure of beam D according to the model. Even though failure did not occur in test of series G, the model suggests that shear capacity was about to reach the shear demand when the test was stopped. It is also noted that the capacity provided by the fibers (V_f) is smaller in these series than in the beams with other series due to the smaller fracture energy and fiber length of shorter fibers.

The previous analysis indicates that shear failures took place when the shear capacity of the compression zone V_c was exhausted after softening of concrete in compression. The shear capacity provided by the fibers through V_f was responsible for 50-60% of shear strength of undamaged specimens at peak load and provided the remaining shear capacity after release of V_c.

4.2. Residual energy absorption capacity

From the experimental observations, it is clear that the use of SFRC significantly increases the energy absorption capacity under both quasi-static and impact loading conditions, which in turn provides more ductility and can be decisive for evacuation and recovery operations, or assessment of rehabilitation possibilities for impact-damaged structures. Moreover, according to residual tests (section 3.4), it becomes clear that the RRI index is not sufficient to provide information about the residual ductility or failure mode. Therefore, a new index concept is proposed here to characterize the residual energy absorption capacity.

Firstly, it is proposed to evaluate the condition of the beams after the impact with an index which does not depend on the measurements taken during the impact test, in order to allow assessing a structure that has suffered an unexpected impact event after it has occurred. The

514 Impact Energy Index (IEI) is proposed to calculate the energy consumed during the impact from
515 the theoretically available energy absorption capacity of an undamaged specimen, denoted A in
516 Fig. 11a. It is noted that the energy actually consumed in the impact is the one listed in Table 3,
517 but it is not a convenient parameter to evaluate damaged structures because of its hard
518 availability. Rather, only the quasi-static undamaged response and the residual deflection after
519 impact are needed to calculate energy A. From the same graphic, A+B represents the total
520 energy absorption capacity of the undamaged test. Accordingly, the IEI is calculated as:
521

522 $$IEI = \frac{A}{A+B} \tag{14}$$

523 After residual testing of impact-damaged specimens, the energy denoted C in Fig. 11b can be
524 calculated, which is the energy absorbed in the residual test. The Residual Energy Index (REI)
525 is introduced to evaluate the energy absorbed in the residual test with respect to that consumed
526 by the corresponding undamaged beam, as follows:
527

528 $$REI = \frac{C}{A+B} \tag{15}$$

529 It has to be noticed that the same ultimate deflection has to be taken to consistently compare
530 results of undamaged and damaged specimens, i.e. the less between residual and undamaged
531 tests has to be considered, as indicated in Fig. 11b. Finally, the total energy absorbed by
532 specimen is evaluated by the Total Energy Index (TEI), suggested as:
533

534 $$TEI = IEI + REI \tag{16}$$

535 In order to analyze the ductility of tested specimens, the three indices have been calculated and
536 they are listed in Table 5. In addition, REI and TEI are represented over IEI in Fig. 12. Different
537 colors have been used to distinguish the failure mode from undamaged to impact-damaged
538 condition in Fig. 12. An interesting trend can be observed for the residual energy capacity as a

function of the damage caused by the impact in Fig. 12a: the REI decreases as the IEI increases in two groups, according to the residual failure mode (brittle or ductile):

$$REI = a + bIEI \tag{17}$$

where the slope of fitted curves has resulted the same (b = -0.12), but parameter a results 0.79 and 0.60 for specimens with residual ductile and brittle response, respectively. The former finding can be useful to predict the residual energy absorption capacity but further experimental research is necessary to fit more reliable curves for the definition of the REI as a function of the IEI. It is also noted that the values of the REI (between 0.45 and 0.85) do not provide itself an easy identification of the residual failure mode or ductility. Here is where the TEI is needed. Once the REI can be calculated from Eq. (17), the TEI can be obtained (Eq. (16)) and its interpretation is more simple as it can be observed in Fig. 12b. TEI values of about 1.0 (0.97-1.15 in Fig. 12b) correspond to the same failure mode of undamaged and damaged beams. For TEI ≥ 1.21, residual tests were ductile in spite of the fact that undamaged specimens failed more brittle by shear. On the contrary, failure changed from ductile for undamaged specimens to brittle for damaged specimens when TEI ≤ 0.85.

According to the above discussion, TEI is a good indicator of the ductility of impact-damaged specimens in comparison with corresponding undamaged beams, but the estimation of REI from Eq. (17) still requires knowing the residual failure mode to choose the appropriate value of parameter a. Further understanding of residual behavior is therefore needed, which is done in the following subsections.

4.3. Residual capacity of resisting mechanisms of impact-damaged beams

From section 4.2 it was concluded that IEI or residual deflection after impact are not enough to predict the residual response of impact-damaged specimens because there are two trends in Fig.

12a. Neither does the criterion by Yoo et al. [26] that the quasi-static undamaged behavior can be used as envelope for residual response, which was valid for their tests with flexural response of both undamaged and damaged specimens. Rather, the residual load carrying capacity and ductility seem to be affected by the crack pattern originated by the impact. According to crack patterns of Fig. 7, two behavioral responses can be observed. On the one hand, without regard of the failure mode under undamaged condition, the specimens without shear plug failed brittle by full development of a shear crack running on one shear span from the point load to the longitudinal tensile reinforcement. The absence of shear plug can be observed by a main vertical crack at midspan section, which was the case of specimens D-STR-IMP-A, D-STR-IMP-B, E-STR-IMP-A, G-STR-IMP-A (Fig. 7). On the other hand, in specimens with a clear shear plug initiation produced by the previous impact, residual failure was ductile regardless of the failure mode of undamaged condition. The shear plug can be observed by one or two major cracks with an inclination larger than 45º degrees at midspan region prior to residual testing, which was the situation of specimens B-STR-IMP-A, C-STR-IMP-B, E-STR-IMP-B, F-STR-IMP, G-STR-IMP-B (Fig. 7). Therefore, it can be concluded that the two regression lines for the REI of Fig. 12a correspond to the presence or absence of shear plug initiation, which can be detected just by observation of specimens after impact.

In order to understand the residual capacity of shear resisting mechanisms, the sequence of one specimen of each failure mode is plotted in Fig. 13. It is observed that brittle failure is associated with the development of a shear crack and it becomes clear how the size of the compression zone progressively reduces to zero. Therefore, the load release obtained in load-deflection diagrams can be due to the destruction of V_c, as undamaged specimens. In contrast, when the impact has initiated a shear plug, the critical section is one (or two) of the two more-or-less symmetrical major cracks defining such shear plug. The crack inclination of such critical cracks ranged from 58º (test G-STR-IMP-B-R) to 70º (test F-STR-IMP-R). The influence of the inclination angle on shear strength can be studied with the model of section 2.2 just by modifying parameter θ_c. The analysis is done in Fig. 14 for test C-STR-IMP-B-R, with an angle

595 of θ_c = 60º according to the experiment. The model results in a significant reduction of V_f with
596 respect to the analysis done with θ_c = 45º (used for undamaged specimens). The shear strength
597 results now (78.0 kN) larger than the experimental maximum load which produced ductile
598 failure (58.5 kN), i.e. the critical section forced by the initiation of shear plug has smaller
599 bending capacity than shear strength. The smaller bending capacity is explained by the damage
600 produced by the impact at both compression and tension zones. The analysis has been repeated
601 for those residual tests with ductile response by introducing in the model the experimentally
602 observed inclination angle θ_c. The results are summarized in Fig. 15, where it is confirmed
603 that the residual strength which produced flexural failure was smaller than the capacity
604 of shear resisting mechanisms of the cracks of the shear plug.
605
606 **5. Conclusions**
607
608 The research presented in this paper has been intended to understand the residual load capacity
609 and ductility of reinforced SFRC beams damaged by a previous impact. An experimental
610 campaign of residual tests of impact-damaged beams has been presented and the results indicate
611 that the residual strength and failure mode depend on the crack pattern produced by the previous
612 impact. Moreover, it has been shown that the residual failure mode and ductility can be rather
613 different than those corresponding to the undamaged condition. Among the results, some
614 specimens presented a more ductile response after being damaged by an impact than without
615 such a damage.
616 The analysis presented in this paper has included a model to evaluate the strength of shear
617 resisting mechanisms, which has been very useful to analyze the contribution of the
618 compression zone and the crack-bridging capacity of SFRC. In addition, new indices have been
619 proposed to understand the energy absorption capacity

According to the experimental results and analyses presented in the paper, the following methodology can be used to evaluate the condition (residual failure mode and energy absorption capacity) of reinforced SFRC beams damaged by an impact event:

a. The theoretical behavior of the specimen in the undamaged condition should be first obtained in terms of a load-deflection diagram. To do this, analytical or numerical models can be used. Of course, research is still open in this field, but the models used in this paper can be of useful help.
b. From the undamaged theoretical response, the energy below the load-deflection curve should be estimated (A+B in Fig. 11a).
c. The residual deflection of the damaged specimen should be measured.
d. The energy consumed by the impact should be calculated (A in Fig. 11a).
e. The IEI is obtained according to Eq. (14).
f. The REI is calculated according to Eq. (17). The appropriate values of parameters *a* and *b* of Eq. (17) are chosen as a function of the presence or not of a shear plug in the damaged specimen. From the REI, the residual energy absorption capacity can be estimated (C in Fig. 11b).
g. The TEI is calculated according to Eq. (16).
h. According to the TEI, the failure mode of the damaged specimen would be:
    - The same as the one under undamaged condition (step a) if TEI = $1.0 \pm \Delta$, where Δ is a tolerance that can be considered as 0.10-0.15 according to the results of the present paper, but further experimentation would be convenient.
    - More ductile than under the undamaged condition if TEI > $1.0 + \Delta$.
    - Less ductile than the undamaged condition if TEI < $1.0 - \Delta$.

Acknowledgement

The financial support provided by the Spanish Research Plans through projects Ref. BIA2012-30998 and BIA2016-74960-R (also with contribution of FEDER funds) is gratefully acknowledged. The authors also thank “Fundación José Entrecanales Ibarra” for funding the PhD fellowship of the second author. The authors express their gratitude to Bekaert for kindly providing the hooked and smooth fibers used in this study.

References

[1] Chen Y, May IM. Reinforced concrete members under drop-weight impacts. Proceedings of the Institution of Civil Engineers: Structures and Buildings 2009;162:45-56.

[2] Kishi KH, Mikami H, Matsuoka KG, Ando T. Impact behavior of shear-failure type RC beams without shear rebar. International Journal of Impact Engineering 2002;27:955-68.

[3] Saatci S, Vecchio FJ. Effects of shear resisting mechanisms on impact behavior of reinforced concrete beams. ACI Structural Journal 2009;106:78-86.

[4] Ulzurrun G, Zanuy C. Enhancement of impact performance of reinforced concrete beams without stirrups by adding steel fibers. Construction and Building Materials 2017;145:166-182.

[5] Hrynyk TD, Vecchio FJ. Behavior of steel fiber-reinforced concrete slabs under impact load. ACI Structural Journal 2014;111:1213-1223.

[6] Zhang J, Maalej M, Quek ST. Performance of hybrid-fiber ECC blast/shelter panels subjected to drop weight impact. Journal of Materials in Civil Engineering 2007;19:855-863.

[7] Adhikary SD, Fujikake K, Li B. State-of-the-art review on low-velocity impact response of reinforced concrete beams. Magazine of Concrete Research 2015;68:701-723.

[8] Bao X, Li B. Residual strength of blast damaged reinforced concrete columns. International Journal of Impact Engineering 2010;37:295-308.

[9] Ulzurrun G, Zanuy C. Flexural response of SFRC under impact loading. Construction and Building Materials 2017;134:397-411.

673 [10] Dinh HH, Parra-Montesinos GJ, Wight JK. Shear strength model for steel fiber reinforced
674 concrete beams without stirrup reinforcement. Journal of Structural Engineering
675 2011;137:1039-1051.
676 [11] Kwak YK, Eberhard MO, Kim WS, Kim J. Shear strength of steel fiber-reinforced concrete
677 beams without stirrups. ACI Structural Journal 2002;99:530-538.
678 [12] Dhakal RP, Wang C, Mander JB. Behavior of steel fibre reinforced concrete in
679 compression. 2005.
680 [13] Kooiman AG, van der Veen C, Walraven JC. Modelling the post-cracking behaviour of
681 steel fibre reinforced concrete for structural purposes. Heron 2000;45:275-307.
682 [14] Dupont D, Vandewalle L. Characterisation of steel fibre concrete with a s-e relation. 2002.
683 Proceedings of the 4th International PhD Symposium in Civil Engineering, Munich. pp. 108-14.
684 [15] Lee SC, Cho JY, Vecchio FJ. Diverse embedment model for steel fibre reinforced concrete
685 in tension: model development. ACI Materials Journal 2011;105:516-25.
686 [16] Chana PS. Investigation of the mechanism of shear failure of reinforced concrete beams.
687 Magazine of Concrete Research 1987;39:196-204.
688 [17] Marí A, Cladera A, Bairán J, Oller E, Ribas C. Shear-flexural strength mechanical model
689 for the design and assessment of reinforced concrete beams subjected to point or distributed
690 loads. Frontiers of Structural and Civil Engineering 2014;8:337-353.
691 [18] Fernández Ruiz M, Muttoni A, Sagaseta J. Shear strength of concrete members without
692 transverse reinforcement: a mechanical approach to consistently account for size and strain
693 effects. Engineering Structures 2015;99:360-372.
694 [19] Reineck KH. Ultimate shear force of structural concrete members without transverse
695 reinforcement derived from a mechanical model. ACI Structural Journal 1991;88:592-602.
696 [20] Muttoni A, Fernández Ruiz M. Shear strength of members without transverse
697 reinforcement as function of critical shear crack width. ACI Structural Journal 2008;105:163-
698 172.
699 [21] Vecchio FJ, Collins MP. The modified compression field theory for reinforced concrete
700 elements subjected to shear. ACI Journal 1986;83:219-231.

701 [22] Gallego JM, Zanuy C, Albajar L. Shear fatigue behaviour of reinforced concrete elements
702 without shear reinforcement. Engineering Structures 2014;79:45-57.
703 [23] Kupfer H, Hilsdorf HK, Rusch H. behaviour of concrete under biaxial stresses. ACI
704 Journal Proceedings 1969;66:656-666.
705 [24] Spanish Ministry for public works. Spanish code for structural concrete. 2008.
706 [25] Adhikary SD, Li B, Fujikake K. Dynamic behavior of reinforced concrete beams under
707 varying rates of concentrated loading. International Journal of Impact Engineering 2012;47:24-
708 38.
709 [26] Yoo DY, Banthia N, Yoon YS. Impact resistance of reinforced ultra-high-performance
710 concrete beams with different steel fibers. ACI Structural Journal 2017;114:113-124.
711
712
713

714 **Figure legends**

715

716 Fig. 1. Sectional analysis: (a) Discretization of cross-section; (b) Material models.

717

718 Fig. 2. Diagonal crack formation.

719

720 Fig. 3. Determination of shear strength: (a) shear resisting mechanisms; (b) stress distributions
721 at the compression zone; (c) Mohr's circle at any point of the compression zone; (d) normal
722 stress distribution at diagonal crack and crack opening; (e) possibilities for the normal stress
723 distributions.

724

725 Fig. 4. Geometry and reinforcement of tested beams.

726

727 Fig. 5. Load-midspan deflection diagrams of quasi-static tests of undamaged beams.

728

729 Fig. 6. Crack pattern after quasi-static tests of undamaged beams.

730

731 Fig. 7. Crack pattern of specimens subjected to residual test, prior and after the residual test.
732 Comparison with corresponding quasi-static undamaged test.

733

734 Fig. 8. Load-midspan deflection diagrams of residual and undamaged tests.

735

736 Fig. 9. Comparison between experimental and model results for undamaged specimens.

737

738 Fig. 10. (a) Measurement of variation of height of cross section at 0.80 m from supports; (b)
739 Comparison of model and experimental cracking load.

740

741 Fig. 11. Definition of energies needed to evaluate energetic index: (a) From quasi-static
742 undamaged response; (b) from residual response.
743
744 Fig. 12. Representation of damage index.
745
746 Fig. 13. Sequence of residual tests of specimens E-STR-IMP-A-R (left) and E-STR-IMP-B-R
747 (right)
748
749 Fig. 14. Analysis of shear capacity of test C-STR-IMP-B-R with an inclination angle of θc =
750 60º.
751
752 Fig. 15. Analysis of shear resisting mechanisms of residual tests with ductile response.

753 **Tables**

754

755 **Table 1.** Summary of material properties of concrete mixtures.

Series ID	Volume fraction	Fiber type	Fiber length/diameter [mm]	Fiber yield strength [MPa]	Compressive strength [MPa]	Indirect tensile strength [MPa]	Fracture energy [kN/m]
A	0%	-	-	-	48.5	4.8	0.28
B	0.5%	Prismatic	60/1	830	59.4	6.1	3.14
C	0.5%	Hooked	60/0.75	1200	61.4	6.7	6.75
D	0.5%	Smooth	10/0.16	3000	64.0	5.4	1.85
E	1.0%	Prismatic	60/1	830	52.1	7.0	6.65
F	1.0%	Hooked	60/0.75	1200	61.3	6.8	9.04
G	1.0%	Smooth	10/0.16	3000	64.7	6.4	4.39

756

757

758

759

760

761

762

763

764

765

766

767

768

769

Table 2. Summary of quasi-static tests of undamaged specimens.

Series	**Test ID**	**Max. load [kN]**	**Energy [kN x m]**
A	A-STR-ST	90	0.62
B	B-STR-ST	133	1.36
C	C-STR-ST	141	2.31
D	D-STR-ST	129	1.89
E	E-STR-ST	138	1.56
F	F-STR-ST	135	2.31
G	G-STR-ST	139	1.66

Table 3. Summary of impact tests. NA: not applicable.

Series	Test ID	Max. load [kN]	Energy [kN x m]	Failure mode	Residual deflection [mm]
A	A-STR-IMP-A	263	0.93	Shear	NA
A	A-STR-IMP-B	289	0.88	Shear	NA
B	B-STR-IMP-A	390	2.04	Flexure	10.0
B	B-STR-IMP-B	392	1.78	Shear	NA
C	C-STR-IMP-A	398	2.24	Shear	NA
C	C-STR-IMP-B	380	2.56	Flexure	13.3
D	D-STR-IMP-A	370	2.46	Flexure	10.9
D	D-STR-IMP-B	419	2.85	Flexure	11.5
E	E-STR-IMP-A	410	2.86	Flexure	9.1
E	E-STR-IMP-B	357	2.38	Flexure	10.0
F	F-STR-IMP	377	2.77	Flexure	10.9
G	G-STR-IMP-A	460	2.16	Flexure	11.4
G	G-STR-IMP-B	468	2.35	Flexure	9.1

800 **Table 4.** Summary of residual tests.

801

Series	Test ID	Max. load [kN]	RRI	Failure mode	Energy [kN x m]
B	B-STR-IMP-A-R	118	0.89	Flexure	4.15
C	C-STR-IMP-B-R	117	0.83	Flexure	3.70
D	D-STR-IMP-A-R	118	0.91	Shear	1.80
D	D-STR-IMP-B-R	127	0.98	Shear	1.16
E	E-STR-IMP-A-R	106	0.77	Shear	1.28
E	E-STR-IMP-B-R	122	0.88	Flexure	3.87
F	F-STR-IMP-R	140	1.04	Flexure	4.88
G	G-STR-IMP-A-R	137	0.99	Shear	2.98
G	G-STR-IMP-B-R	136	0.98	Flexure	4.12

802

803

804

805

806

807

808

809

810

811

812

813

814

815

816 **Table 5.** Energy index.

817

Series	Test ID	IEI	REI	TEI
B	B-STR-IMP-A-R	0.60	0.76	1.35
C	C-STR-IMP-B-R	0.65	0.60	1.25
D	D-STR-IMP-A-R	0.59	0.56	1.15
D	D-STR-IMP-B-R	0.60	0.45	1.05
E	E-STR-IMP-A-R	0.54	0.58	1.12
E	E-STR-IMP-B-R	0.56	0.85	1.41
F	F-STR-IMP-R	0.23	0.74	0.97
G	G-STR-IMP-A-R	0.30	0.55	0.85
G	G-STR-IMP-B-R	0.25	0.76	1.01

818

819

Figures

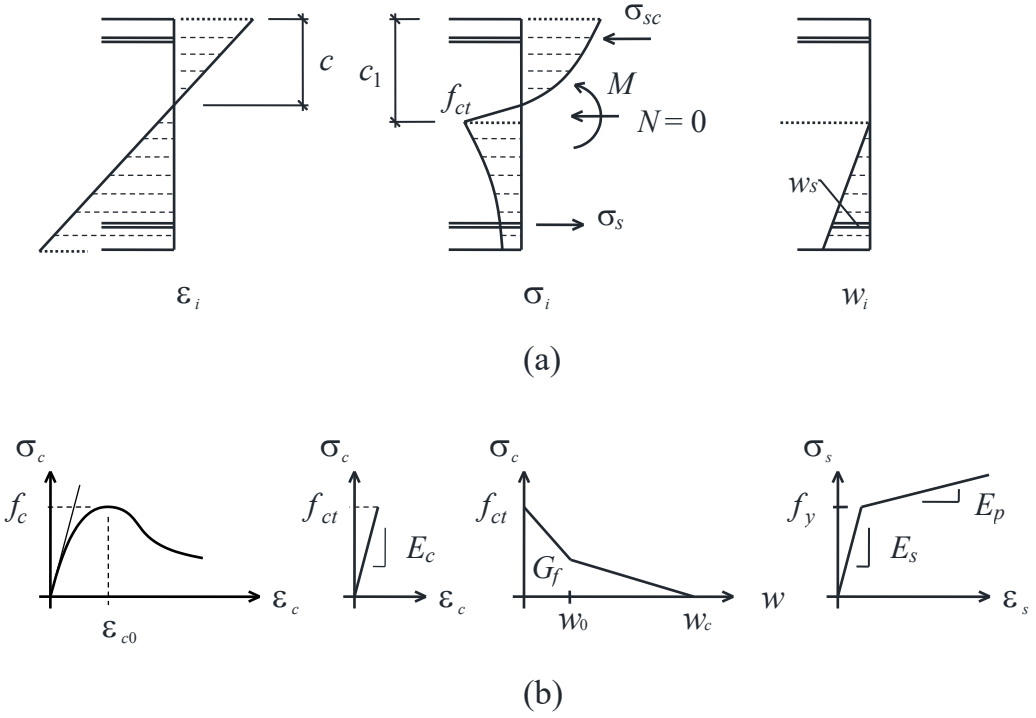

Fig. 1. Sectional analysis: (a) Discretization of cross-section; (b) Material models.

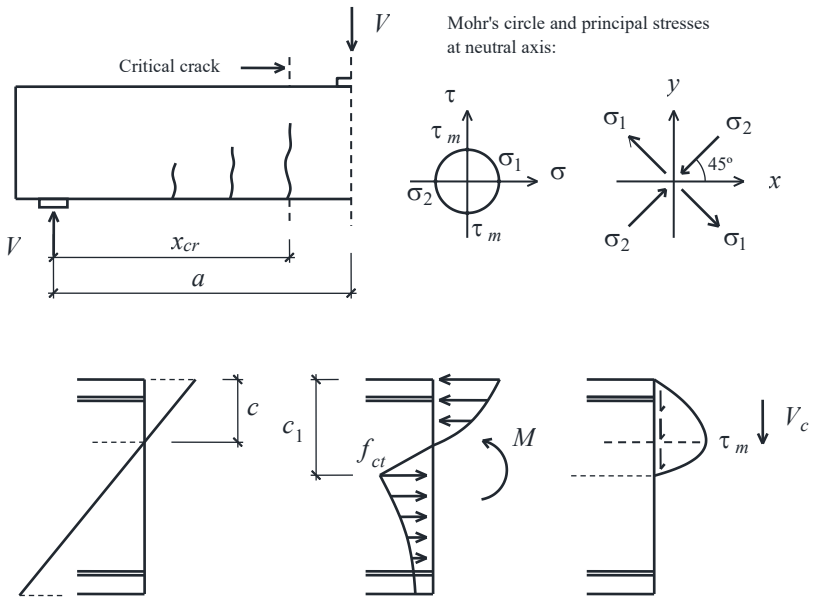

Fig. 2. Diagonal crack formation.

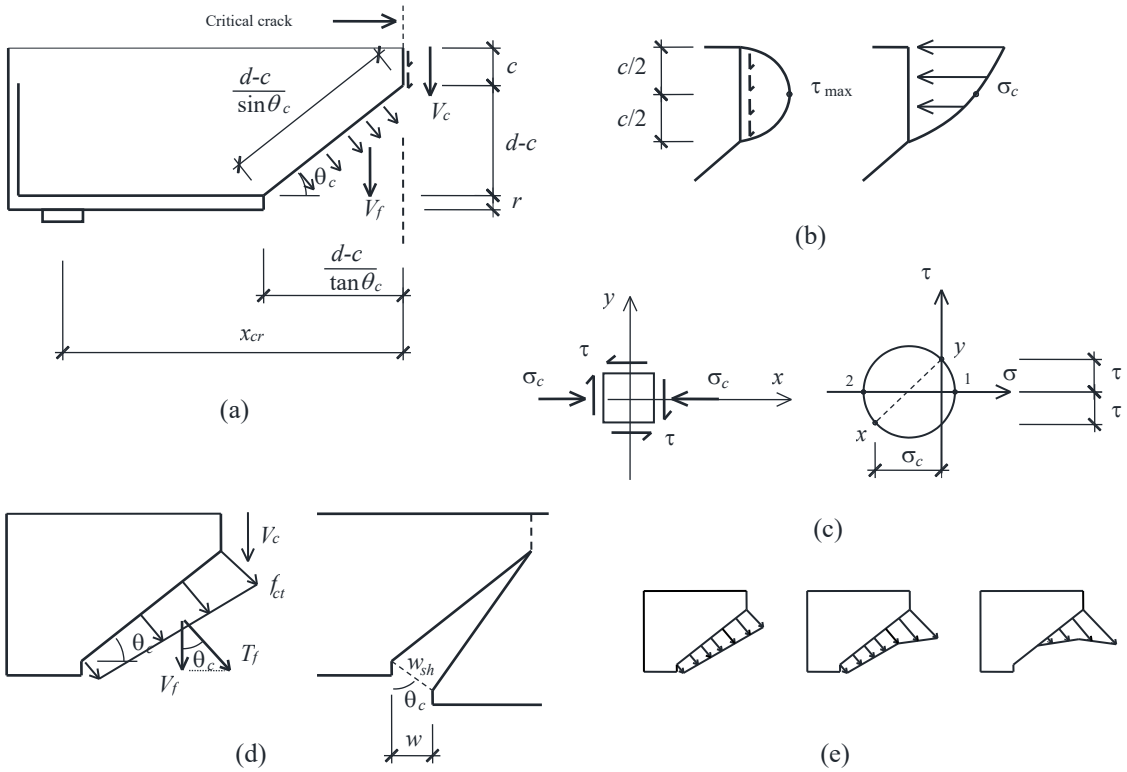

Fig. 3. Determination of shear strength: (a) shear resisting mechanisms; (b) stress distributions at the compression zone; (c) Mohr's circle at any point of the compression zone; (d) normal stress distribution at diagonal crack and crack opening; (e) possibilities for the normal stress distributions.

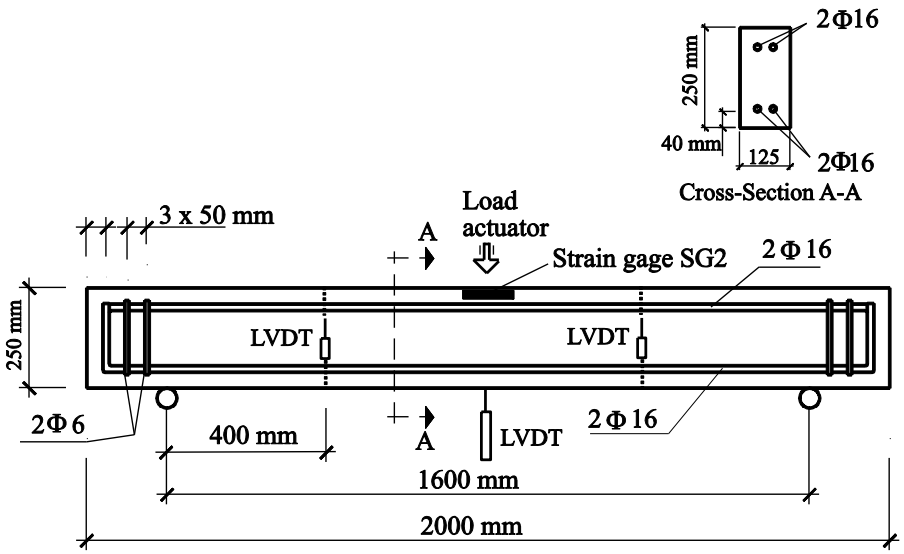

Fig. 4. Geometry and reinforcement of tested beams.

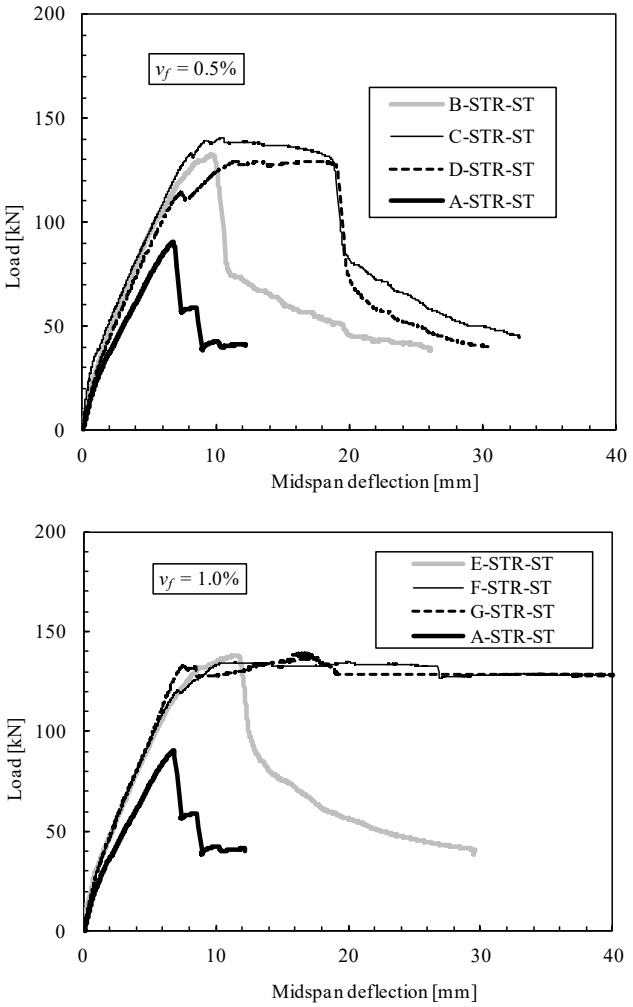

Fig. 5. Load-midspan deflection diagrams of quasi-static tests of undamaged beams.

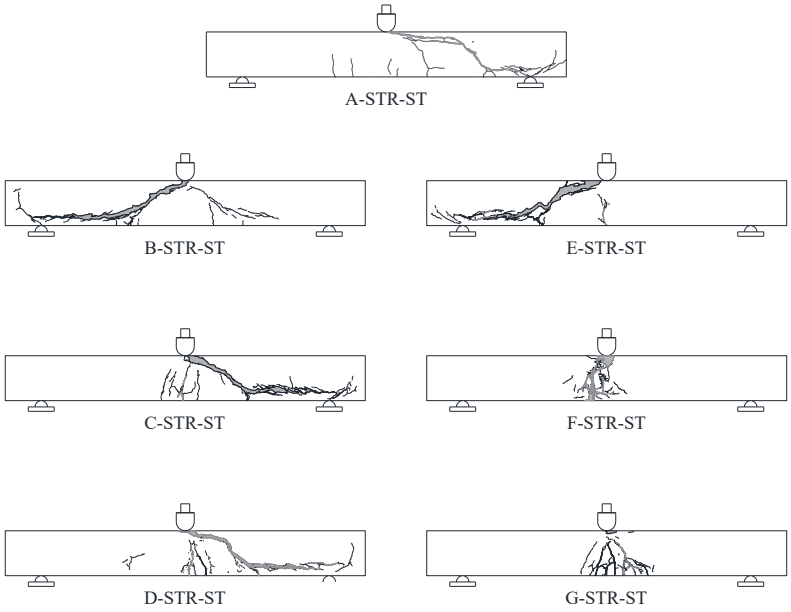

Fig. 6. Crack pattern after quasi-static tests of undamaged beams.

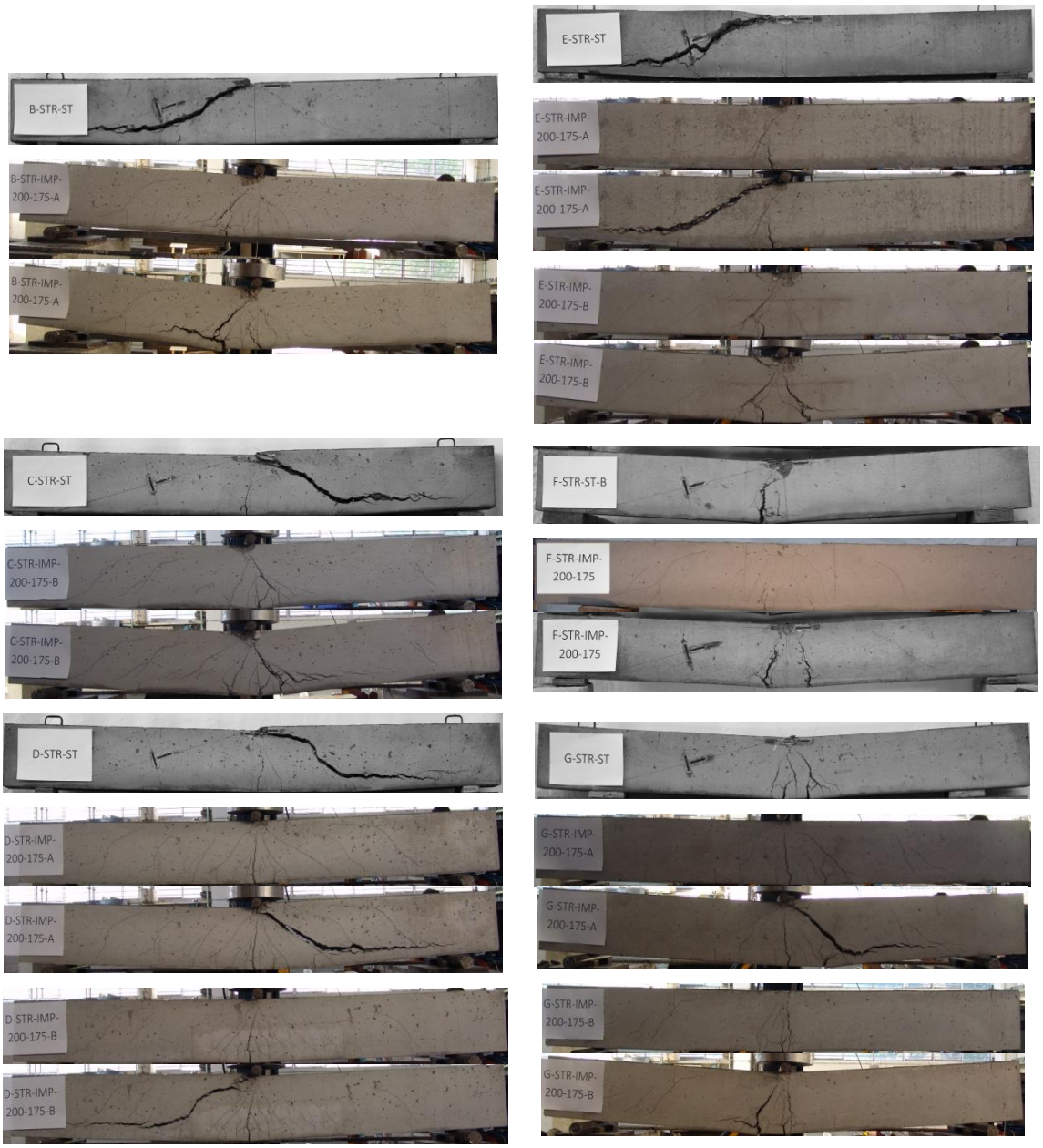

900 **Fig. 7.** Crack pattern of specimens subjected to residual test, prior and after the residual test.
901 Comparison with corresponding quasi-static undamaged test.

902

903

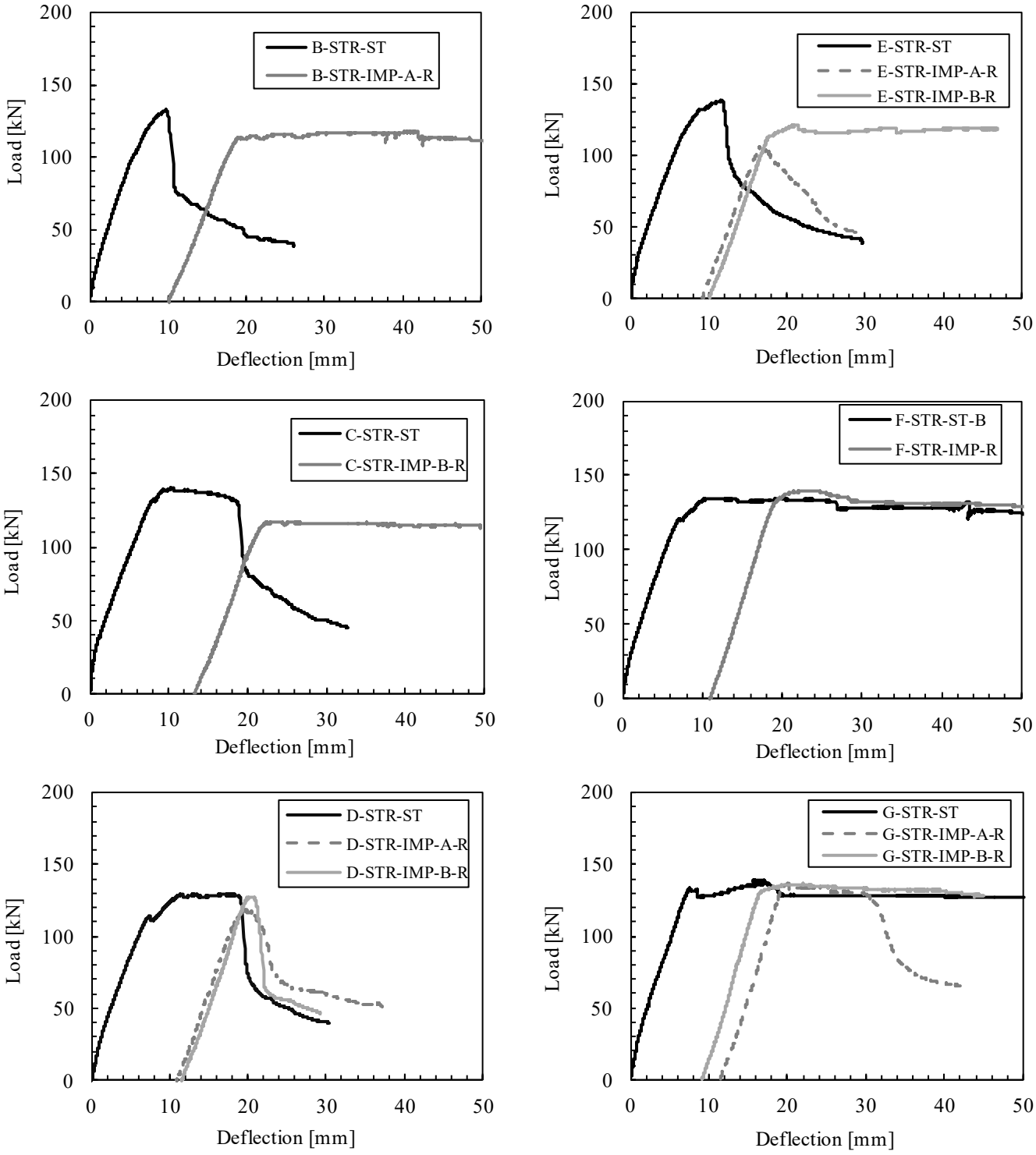

904 **Fig. 8.** Load-midspan deflection diagrams of residual and undamaged tests.

905

906

907

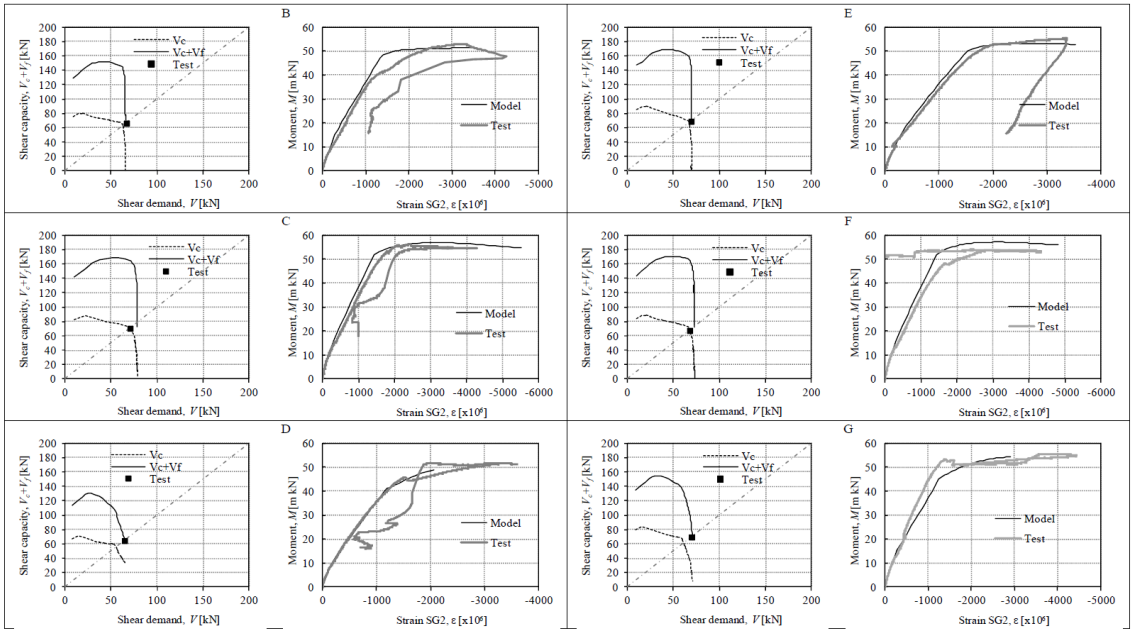

Fig. 9. Comparison between experimental and model results for undamaged specimens.

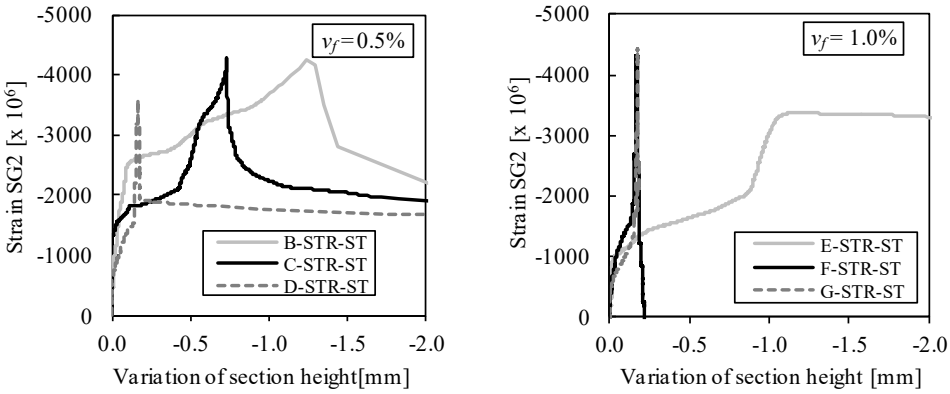

(a)

Series	P_{cr} [kN] Experimental	P_{cr} [kN] Model
B	80	90.3
C	108	102.1
D	72	77.4
E	85	104.6
F	110	101.1
G	88	90.8

(b)

Fig. 10. (a) Measurement of variation of height of cross section at 0.80 m from supports; (b) Comparison of model and experimental cracking load.

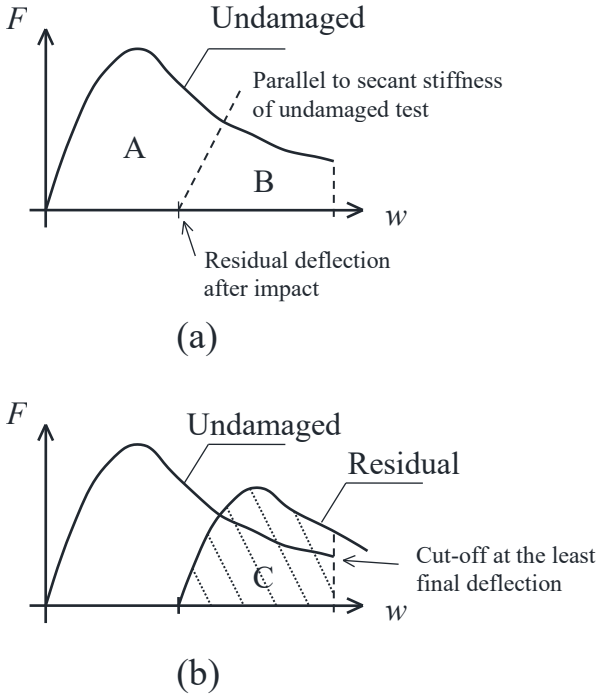

Fig. 11. Definition of energies needed to evaluate energetic index: (a) From quasi-static undamaged response; (b) from residual response.

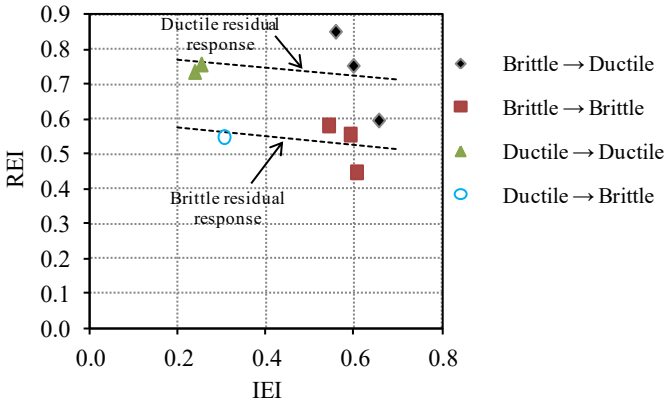

(a)

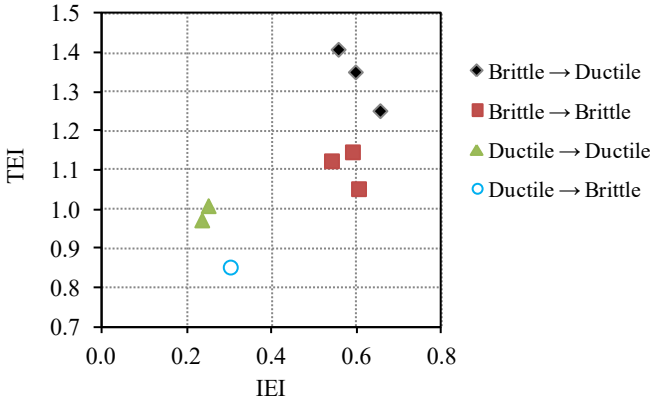

(b)

Fig. 12. Representation of damage index.

Fig. 13. Sequence of residual tests of specimens E-STR-IMP-A-R (left) and E-STR-IMP-B-R (right)

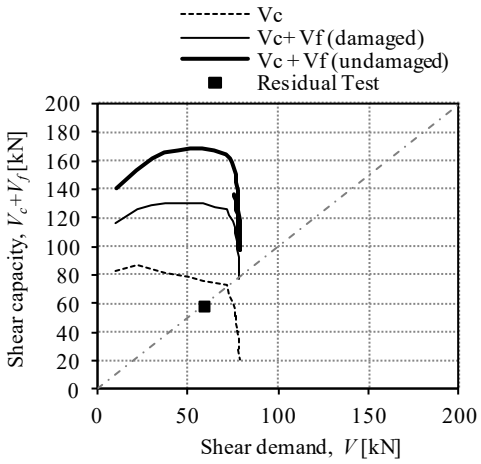

Fig. 14. Analysis of shear capacity of test C-STR-IMP-B-R with an inclination angle of θ_c = 60º.

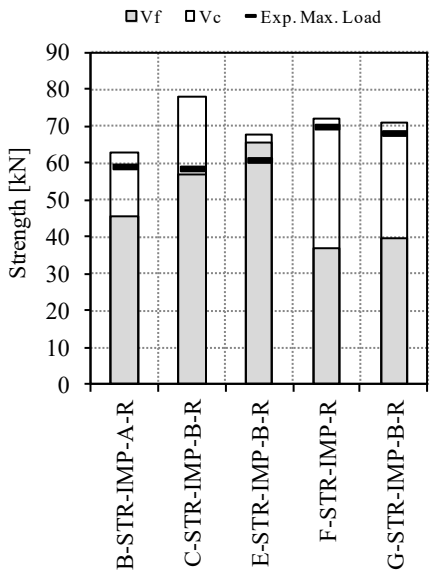

Fig. 15. Analysis of shear resisting mechanisms of residual tests with ductile response.